DOI: 10.13009/EUCASS2017-91

DOI: ADD DOINUMBER HERE

Comparison of a Closed-Loop Control by Means of High-Fidelity and Low-Fidelity Coupled CFD/RBD Computations

Marius Franze⋆
⋆*DLR, German Aerospace Center, Institute of Aerodynamics and Flow Technology*
Brunswick, D-38108, Germany
marius.franze@dlr.de

Abstract

This work compares the principle of a basic fin-controlled sounding rocket with coupled computational fluid dynamic and rigid body dynamic simulations of two coupling environments: (1) a low-fidelity approach using Missile DATCOM as semi-empirical aerodynamic solver, and (2) a high-fidelity approach using DLR TAU as URANS CFD code. The flight mechanics solver REENT is used in both cases. A closed-loop flight path control is developed and adjusted via low-fi simulations and then verified via high-fi simulations. For simple roll and pitching maneuvers the environments match good, whereas differences can be expected in complex maneuvers, e.g. body-body interactions or separation procedures.

Nomenclature

α	=	angle of attack [°]	h	=	altitude [km]
γ	=	flight path angle [°]	F_x	=	Thrust in x-direction [N]
ϵ	=	relative error [%]	M	=	Mach number [1]
η	=	horizontal fin deflection [°]	p	=	pressure [Pa]
μ	=	bank angle [°]	K	=	Gain factor [1]
ξ	=	vertical fin deflection [°]	t	=	flight time [s]
ρ	=	density [kg/m^3]	v	=	velocity [m/s]
χ	=	flight path heading [°]	x_{CoG}	=	Center of gravity [m]
ω_x	=	roll rate [Hz]	$\vec{X}_{t_n}$	=	State vector
$(...)_C$	=	Coarse Mesh	RMD	=	Reent - Missile DATCOM
$(...)_F$	=	Fine Mesh	RT	=	Reent - DLR TAU
$(...)_T$	=	Target value	SOSE	=	Second Order Shock Expansion

1. Introduction

In real life applications flight vehicles rarely fly uncontrolled, from big aircrafts like an Airbus 380 down to small rockets like AIM-9 Sidewinder. Usually the controller is developed and adjusted using complex look-up-tables containing aerodynamic coefficients for several flight points where the dynamic derivatives get calculated from. This procedure is very computational intensive, in terms of time as well as cost, because these tables exceed hundreds of entries in the most cases. Especially during the preliminary design phase of flight vehicles these tables needs to be calculated from scratch when the design parameter change, e.g. during geometry variations.

On this account there is ongoing work investigating the possibility to virtually fly the real life controller setup as soon as possible. Several papers used coupled high-fidelity CFD calculations with flight mechanic solvers to realistically predict controlled maneuvers like roll, pitch movements. Costello and Sahu[4] for example developed a basic method to predict the derivatives using a CFD/RBD coupled free-oscillation method. Afterwards Sahu et.al.[12] controlled the flight motion using small jets and their interactions on the projectile surface and later on Sahu[11] as well as Silton et.al.[14] extended their coupled method with rotating canards via moving grids. Especially the last mentioned

Copyright © 2017 by Marius Franze. Published by the EUCASS association with permission.

DOI: 10.13009/EUCASS2017-91

paper is rather similar to the high-fidelity coupled method presented in this paper as both use moving grid techniques on controlled rockets in a basic configuration.

The first section presents the used configuration as well as the applied numeric codes and compares their solution methods. The second part analyses the calculated results and compares the two different coupled procedures using a controlled rolling, pitching and flight path motion. Finally a summary of the collected results and an outlook for future proceeding is given.

2. Solution Technique

2.1 Aerodynamic Solver DLR TAU

The unsteady Euler equations including rigid body motion are solved using the DLR TAU code which is validated for subsonic, transonic and hypersonic flows.[13,10] The completely parallelized code uses domain decompositioning via Message Passing Interface (MPI). Due to the chosen high amounts of analyzed timesteps, only inviscid unsteady Euler equation calculations were applied, although the DLR TAU Code is capable of unsteady viscous Navier-Stokes equation calculations. With increasing Mach number the viscous components of the forces will be negligible compared to the pressure induced components.

A second order AUSMDV[19] upwind scheme with backward euler relaxation solver is used for the whole trajectory. Computing 500 iterations per unsteady dual time step of $\Delta t = 0.02s$, the density residual reaches values below $Res < 2 \cdot 10^{-4}$ to get a solution with converged aerodynamic coefficients.

The following computations are produced with a free-oscillation flight by means of its position, orientation, flight velocity and roll rates, with unsteady DLR TAU as well as steady Missile DATCOM computations, changing the flight condition every time step $\Delta t = 0.02s$. For this use case of the DLR TAU code an external motion function was applied, were the grid itself is moving.[9] This function allows to set the inflow condition to $M = 0$ and move the mesh with a given velocity in a virtual endless computation area. As a result the inflow flux correlates to the given relative velocity, which in the end produces surface loads, similar to the commonly used inflow condition $M \neq 0$.

2.2 Semi-empirical Solver Missile DATCOM

Missile DATCOM is a semi-empirical tool mainly used for preliminary design and performance prediction of rocket like flight vehicles. To calculate the force and moment coefficients at high Mach numbers the program uses a Second-Order-Shock-Expansion (SOSE) method with a Van Driest-II method, which is just valid for high Mach numbers and small angle of attack. At lower Mach number especially in the subsonic region Missile DATCOM mainly uses look-up tables as described in the documentation.[17,18,1]

2.3 Flight Mechanics Solver REENT

REENT is originally developed by the University of Stuttgart in 2001[2] and in the following years amongst others enhanced by the DLR, Brunswick, Institute for Aerodynamic and Flow Technology, Spacecrafts Department.[5,3,7]

It solves the equations of motion in three and six degree-of-freedom (DOF) simulations with respect to the resulting forces and moments from the vehicle resulting in a flight path over time. Several gravitational models as well as earth models are implemented. REENT contains diverse analytic atmospheric models, e.g. US standard atmosphere 1962,[16] MSISE 1990[8] as well as the possibility to read them from a given table.

As it computes with respect to the earth central coordinate system, the program has evolved to a powerful trajectory and reentry simulation tool especially for the preliminary design phase.

2.4 Model Geometry and Initial Conditions

The computed vehicle is shown in figure 1. It is a basic generic rocket with flare and four fins in cross configuration. Table 1 contains the main vehicle parameters. The purpose of the configuration is to show the principle of the implemented coupling and control procedure.

The initial starting conditions are adjusted according to minimize external effects. For example, during the tuning of the PID controller for the rolling motion a flight path angle of $\gamma = 90°$ without thrust $F_x = 0kN$ along x-direction is used to exclude pitching, yawing and acceleration effects as much as possible. Further, a high Mach number of $M = 5.13$ is chosen, because of the computation assumptions for the aerodynamic SOSE solver of Missile DATCOM.

DOI: 10.13009/EUCASS2017-91

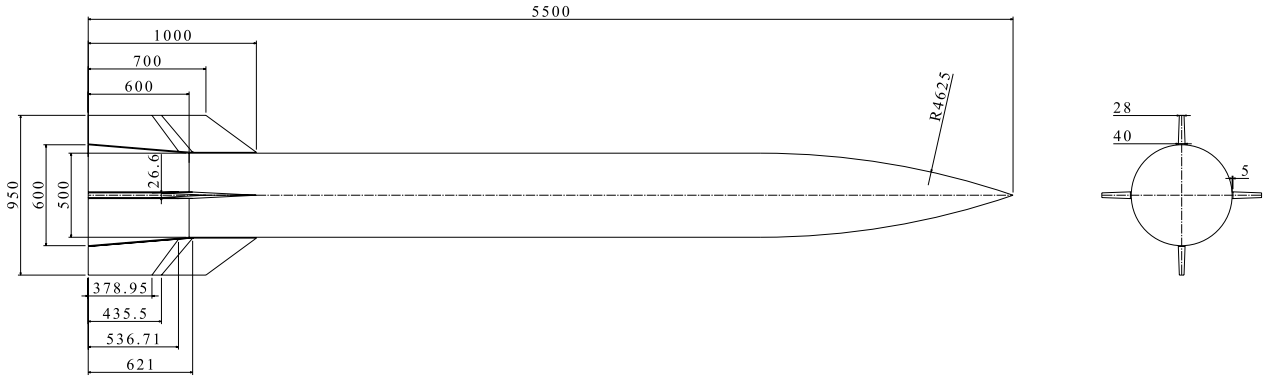

Figure 1: Schematic representation of the basic finned vehicle.

Table 1: Rocket parameters.

Parameter	Symbol	Value
Mass	m	500 kg/m^3
Center of gravity in x	x_{CoG}	2.2 m
Moment of inertia in x	I_{xx}	34.6 $kg \cdot m^2$
Moment of inertia in y	I_{yy}	1982.5 $kg \cdot m^2$
Moment of inertia in z	I_{zz}	1982.5 $kg \cdot m^2$
Mach number	M	5.13
Flight path angle	γ	0 or 90 °
Thrust in x	F_x	0 or 5 kN
Altitude over WGS84	h	20 km

As described in chapter 2 2.2 the accuracy is better at applications in hypersonic flow. During the vertical flight the rising altitude results in decreasing atmosphere pressure and density as described in the analytic US standard atmosphere model from 1962 called US62.[16] Therefore the aerodynamic forces and moments continuously reduce to zero. For this reasons the thrust in x-direction is set to $F_x = 0kN$, i.e. the rocket is not accelerating in roll axis direction due to thrust. Thus the computation is at altitudes with an atmosphere which is dense enough to produce controlling moments through the fins.

For the later application of pitching and flight path control a flight path angle of $\gamma = 0°$ with a thrust $F_x = 5kN$ is applied, meaning horizontal flight with a small amount of acceleration in roll axis direction.

2.5 Coupling Procedure

As an overview figure 2 illustrates the coupling procedure between the exchangeable aerodynamic solvers DLR TAU or Missile DATCOM and the flight mechanic solver REENT via a Python interface.

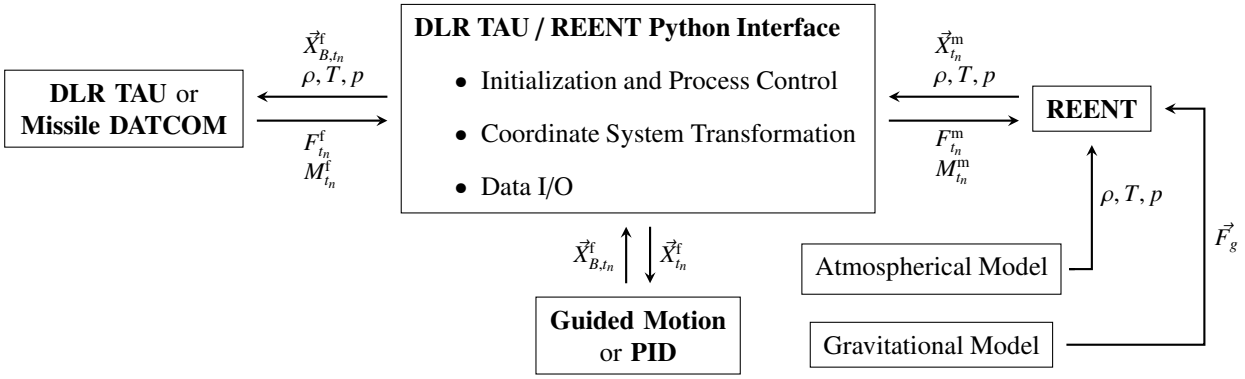

Figure 2: Overview of coupled modules.

DOI: 10.13009/EUCASS2017-91

The Python interface exchanges the state vector $\vec{X}_{t_0}$, shown in equation 1, given from REENT to the chosen aerodynamic solver in their needed coordinate system and receives the calculated forces and moments coefficients which again get looped back into the flight mechanic program. The loop is closed.

Between the exchange of the state vector a Python module contains the controller input for the applied controlling surfaces or force vectors resulting from imaginary thrusters. This module modifies the given state vector for the vehicle and each movable control surface resulting in the total state vector for each block $\vec{X}_{B,t_n}$ at time step t_n. The controller can be included by using a black box executable program or a simple PID controller. The latter is used in this work.

Meanwhile in each time step the current atmospheric values regarding density ρ, temperature T as well as outer pressure p are transferred to the flow solver adjusting the farfield conditions. With this method the farfield contains an atmospheric profile of the given parameters as seen in the real flight.

The state vector $\vec{X}_{t_0}$ contains all four motion parameters resulting in a six DOF simulation:

$$\vec{X}_{t_0} = \left(\underbrace{r, \lambda, \delta}_{Position}, \underbrace{v, \gamma, \chi}_{Velocity}, \underbrace{\alpha, \beta, \mu}_{Orientation}, \underbrace{\omega_x, \omega_y, \omega_z}_{RotationalMotion} \right), \tag{1}$$

where the components are derived from positions with respect to the Earth-Centered-Earth-Fixed (ECEF) frame, velocity in the horizontal frame, orientation in the aerodynamic frame and rotation rates in the body frame.

The coupling procedure, shown in figure 3, is a loosely coupled method analogue to the Improved Parallel Staggered (IPS) scheme presented by Farhat and Lesoinne.[6]

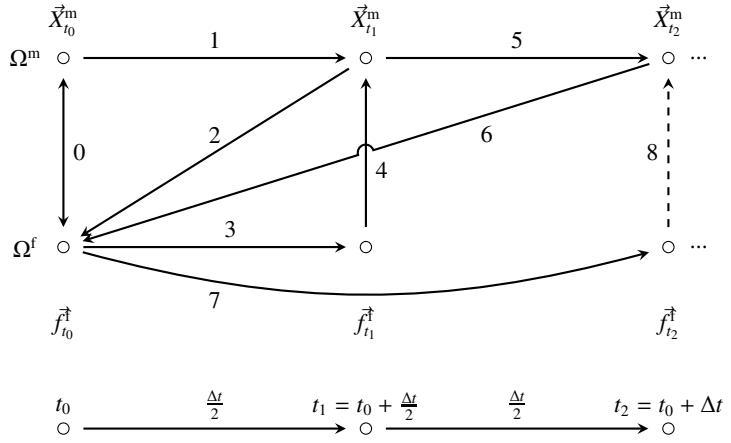

Figure 3: Coupling procedure similar to IPS after Farhat and Lesoinne.[6]

First the flight mechanic domain Ω^m starting vector $\vec{X}_{t_0}$ is transferred to the flow solver domain Ω^f which calculates the steady aerodynamic forces and moments, denoted as interchange step 0. On this basis the flight mechanics solver calculates its first half time step (step 1) and transfers the new vector back to the flow solver (step 2). In this work, REENT uses a second order Runge-Kutta method with half time steps for better accuracy. The aerodynamic solver produces values (step 3) for the supporting point of REENT (step 4), but calculates the resulting flight path based on the full time steps (step 7), which is calculated (step 5) and given (step 6) by REENT. As shown in Farhat and Lesoinne,[6] this method allows bigger time steps which saves computation time.

2.6 Control Process and Design of the PID Controller

As the main intention of this work is not to design a high performance highly agile controller for launched projectiles, but rather to show the basic procedure of a possible design process with interchangeable aerodynamic solver, a simple PID controller was applied as shown in figure 4 by means of a roll motion control. It illustrates the scheme in feedback configuration with discretely proportional (P), integral (I) and derivative (D) part and their corresponding gain factors K_p, K_i and K_D respectively.

The current work uses the vertical fin pair (ξ_1 and ξ_3) to control the roll motion μ in the first place as well as the flight path heading χ in the second place. The flight path angle γ get controlled via the horizontal fin pair (η_2 and η_4).

DOI: 10.13009/EUCASS2017-91

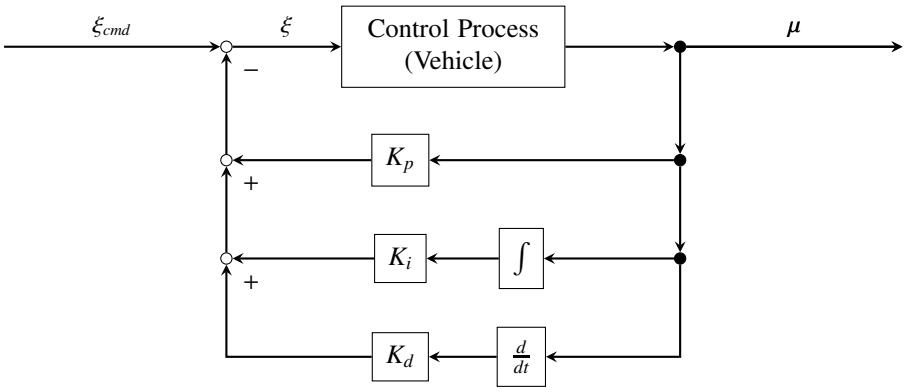

Figure 4: PID control of rolling motion in feedback configuration.

2.7 Design of the PID Controller

The PID controller is designed according to the first adjustment method from Ziegler-Nichols.[20] It is an heuristic method, which means that it is per definition not an optimal controller, but suits the given tasks very good, as shown in figure 5. This plot is a result of a Reent-Missile DATCOM (RMD) coupling method for the sake of small computation times.

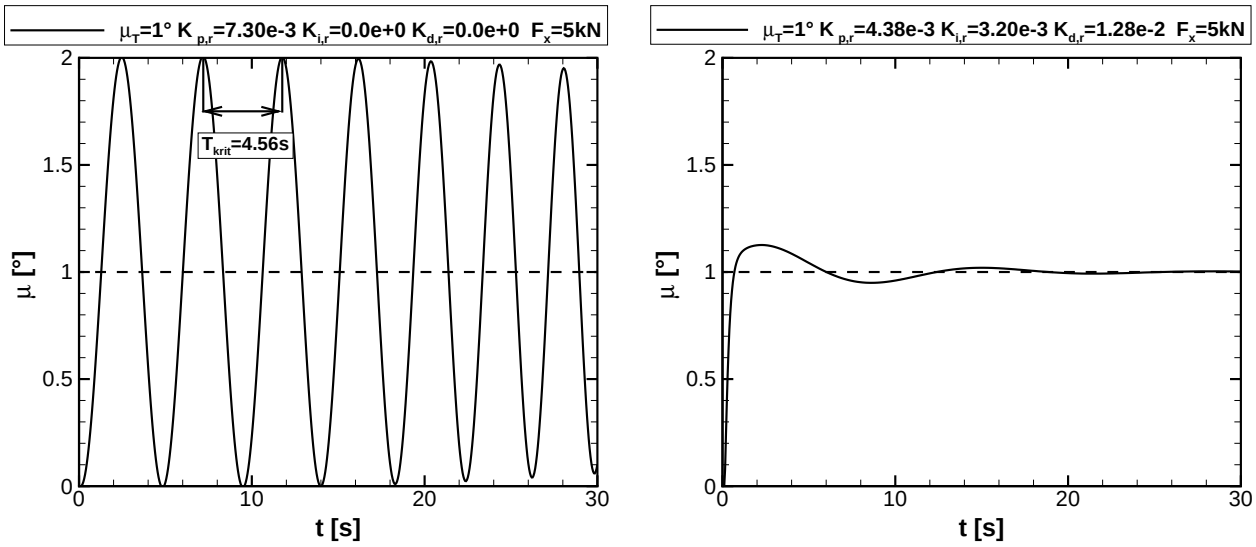

(a) Critical P-controller behavior.

(b) After the application of Ziegler and Nichols equations.

Figure 5: PID controller design after Ziegler-Nichols method[20] for the rolling motion using RMD coupling.

First, one computes the critical proportional gain factor $K_{p,crit}$ to the point, where a continuously oscillation is the control answer, like it is shown in figure 5(a). Afterwards the critical periodlength T_{krit} is measured and the following equations are applied to compute the resulting gain factors (equation 2, 3 and 4).

$$K_p = 0.6 \cdot K_{p,crit} \tag{2}$$

$$K_i = \frac{K_{p,crit}}{0.5 \cdot T_{crit}} \tag{3}$$

$$K_d = \frac{K_{p,crit}}{0.125 \cdot T_{crit}} \tag{4}$$

The resulting controlled roll motion is shown in figure 5(b), which shows the typical overshoot after the first target crossing followed by asymptotic convergence to the target value. This procedure is applied for the longitudinal pitch motion as well.

DOI: 10.13009/EUCASS2017-91

2.8 Mesh Convergence Study

2.8.1 DLR TAU

Table 2 compares the two applied meshes. Regarding the force coefficient in x-direction C_x there is a small difference of 0.004%, although the fine mesh has more than twice the number of points. Figure 6 illustrates, that the raising number of points is mainly due to the near surface field, were the resolution is highly increased from figure 6(a) to 6(b). A proper resolution of the near surface is important for this kind of simulation were the far surface mesh size can be increased rapidly to save computation time, because a better resolved shock far away from the surface does not influence the forces and moment coefficients.

Table 2: Mesh convergence study.

Mesh	**Points [-]**	**C$_{fx}$ [-]**
Fine F	967961	-0.23863
Coarse C	438276	-0.23864
Percentage	54.7%	0.004%

Overall the differences after $\Delta t = 11s$ CDF/RBD coupled flight time is $\Delta\omega_x = 0.8\%$ at $\omega_x = 1.38Hz$ and $\Delta x_{CoG} = 0.2m$. For the following DLR TAU computations the coarse mesh is used.

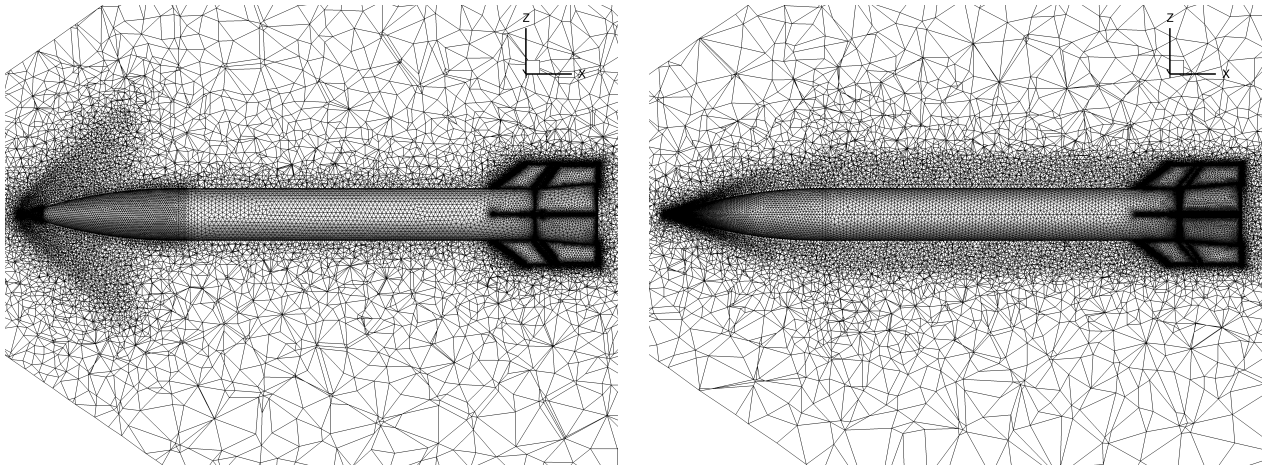

(a) Coarse Mesh. (b) Fine Mesh.

Figure 6: Mesh topology for grid convergence study.

2.8.2 Missile DATCOM

As Missile DATCOM uses a SOSE method, it computes the resulting forces and moments on a surface representation shown in figure 7.

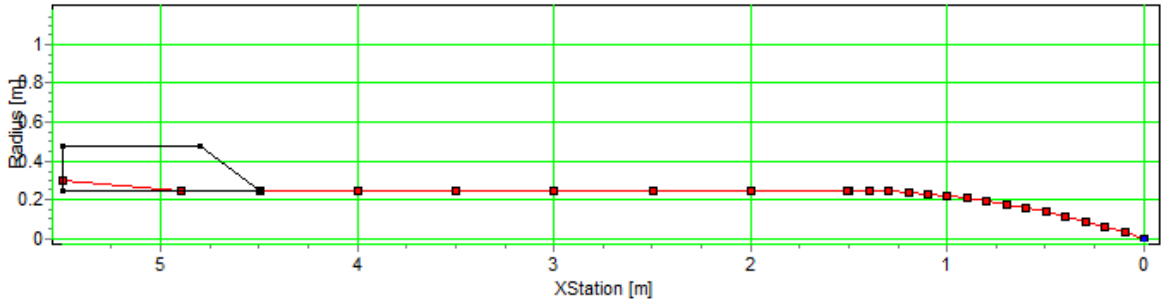

Figure 7: Paneled representation of basic finned vehicle in Missile DATCOM.

DOI: 10.13009/EUCASS2017-91

If the important geometric features, like flare, rounding of the ogive front as well as the fin geometry are reasonably modeled, there is no need for a mesh convergence study. Missile DATCOM is able to achieve good results for the given geometry and Mach number with an estimated error of about 10% compared to experimental data.[15]

2.9 Plausibility Study

Table 3 describes the two mesh converged solutions for a normal mesh and a moving fin chimera mesh. At first the huge number of points for the chimera mesh are noticeable. They result from the necessary interpolation region shown in figure 8.

Table 3: Normal vs. chimera mesh with fin deflection angle $\eta = 0.3°$.

Mesh	Points [-]	C_{fx} [-]
Coarse	438276	-0.235956
Chimera	6469099	-0.234665
Percentage	1476%	0.55%

The *black* mesh shown in figure 8(a) is the mesh of the main body, while the *red* mesh is the mesh of each separate fin. One can easily see the gap of $5mm$ between the fins and the main body as well as the refined farfield mainly around the bodies. Often the gap is an unwanted trade off to use the chimera technique but in this work it is a realistic representation of the problem because a build rocket with moving fins would have a discrete gap as well.

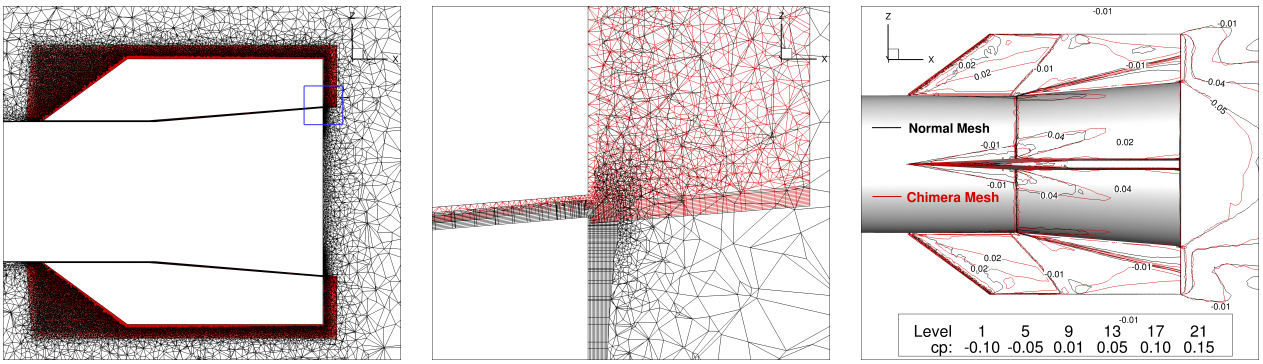

(a) Tail view of chimera blocks.

(b) Detailed view of gap between fins and main body.

(c) Pressure distribution with and without chimera mesh.

Figure 8: Mesh view of chimera interpolation region with main body mesh in *black* and fin mesh in *red* including the prism layer in the gap between.

The gap between the bodies is filled with prismatic layers as illustrated in the detailed view of figure 8(b). These regions need a very fine resolved mesh which leads to the significantly increase of points compared to a mesh without chimera technique. On the other hand this method allows to freely move and rotate the five generated mesh blocks independently from each other. This is achieved by the controller of the guided motion module shown in figure 2.

The difference in force coefficient in x-direction between the normal and the chimera mesh is less than 0.55% with no angle of attack $\alpha = 0°$, sideslip $\beta = 0°$ and Mach number $M = 5.13$, which is supported in the small differences in the pressure distribution shown in figure 8(c).

Figure 9 compares the resulting motions of a fixed fin mesh with a moved chimera block mesh. For this plot the fins in the chimera mesh are rotated linearly deflecting from $\eta = 0°$ to $\eta = 0.3°$ in a time window from $t = 0s$ to $t = 2s$.

The resulting rolling moment coefficient C_{mx} (figure 9(a)) shows the good agreement between the two meshes and the falling of the coefficient in the case of the fixed fin mesh, as the difference between the final and the initial roll rate gets smaller and smaller with increasing flight time. Beginning from $t = 2s$, the fins have a fin deflection angle of $\eta = 0.3°$ in both cases and the values of C_{mx} agree very well.

The final roll rate at the end of the computation (figure 9(b)) differs because of the thinner atmosphere as this test case is flying with $M = 5.13$ vertically away from the center of the earth. The constant atmosphere plots have their start value from the initial starting altitude of $h = 20km$, leaving atmospheric pressure and density constant. The result is a higher rolling moment and roll rate due to the increased aerodynamic forces.

DOI: 10.13009/EUCASS2017-91

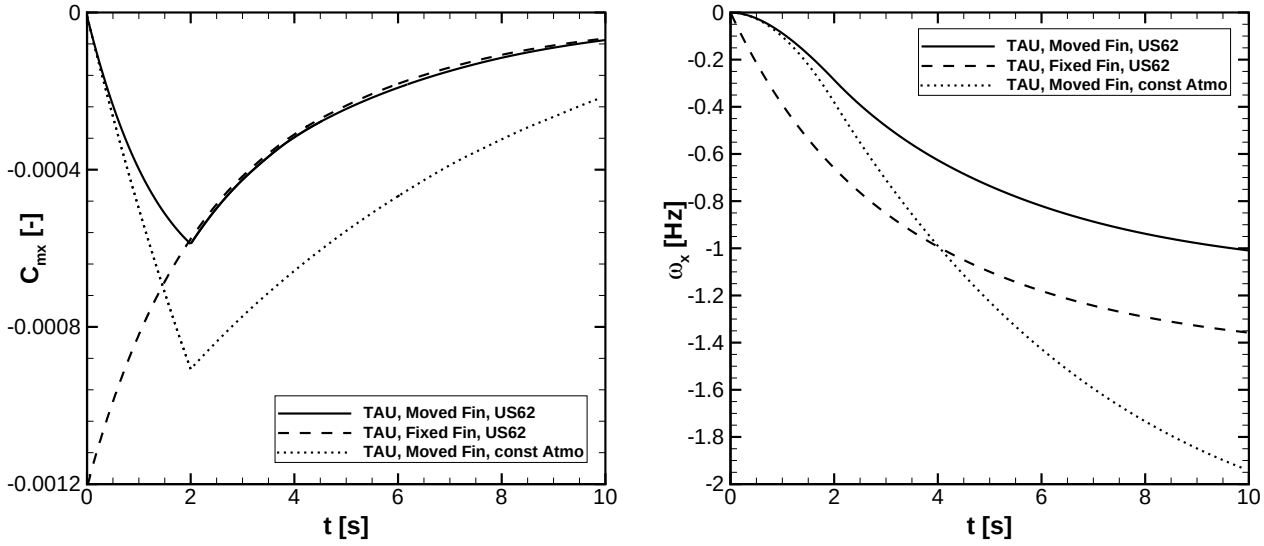

(a) Roll moment coefficient for different fin and atmosphere models.

(b) Roll rate development for different fin and atmosphere models.

Figure 9: Fixed and moved fin roll development for constant and analytic atmospheres.

3. Results of Analysis

3.1 Control of the Rolling Motion

The discussed computation starts with an initial flight path angle $\gamma = 0°$ and without thrust $F_x = 0kN$, otherwise the atmosphere is too thin to get reasonable control surface forces and moments after significant flight time. The resulting roll motion in figure 10 shows a very robust behavior of the PID controller. Over the whole controlling range of the targeted roll angle $\mu_T = 0°$ to $\mu_T = 180°$ the developed flight has an error of less than $\epsilon < 3\%$ after the second cross of the target value at a flight time of $t = 25s$. With raising target roll values μ_T the overshoot behavior increases from $\epsilon = 13\%$ to $\epsilon = 51\%$ leaving the relative error after $\Delta t = 25s$ almost unaffected.

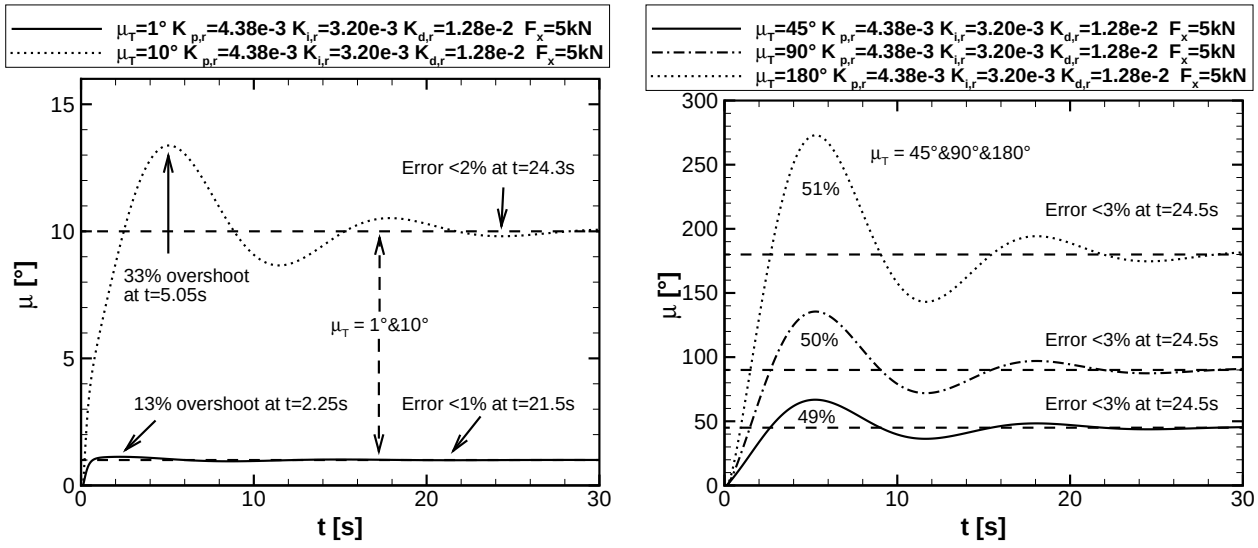

(a) Roll motion for $\mu_T = 1°, 10°$.

(b) Roll motion for $\mu_T = 45°, 90°, 180°$.

Figure 10: Roll motion answer for different roll target values μ_T.

The described roll motion controller is then applied during the Reent-DLR Tau (RT) coupling. Figure 11 shows the two coupling schemes RT and RMD in comparison. The overall agreement of the rolling motion in figure 11(a) is good, proofing again the very robust controller, which got implemented. The overshoot behavior increases from RT

DOI: 10.13009/EUCASS2017-91

to RMD indicating that the fin develops a higher controlling force and moment with the high-fidelity flow solver. The raising error after $t = 25s$ backs this fact.

The velocity plots in figure 11(b) again show that the computed drag force is predicted higher in the DLR TAU code. Additionally to the higher accuracy of the computation, DLR TAU captures inertia forces of the fluid itself adding to the controlling force which can not be calculated within Missile DATCOM.

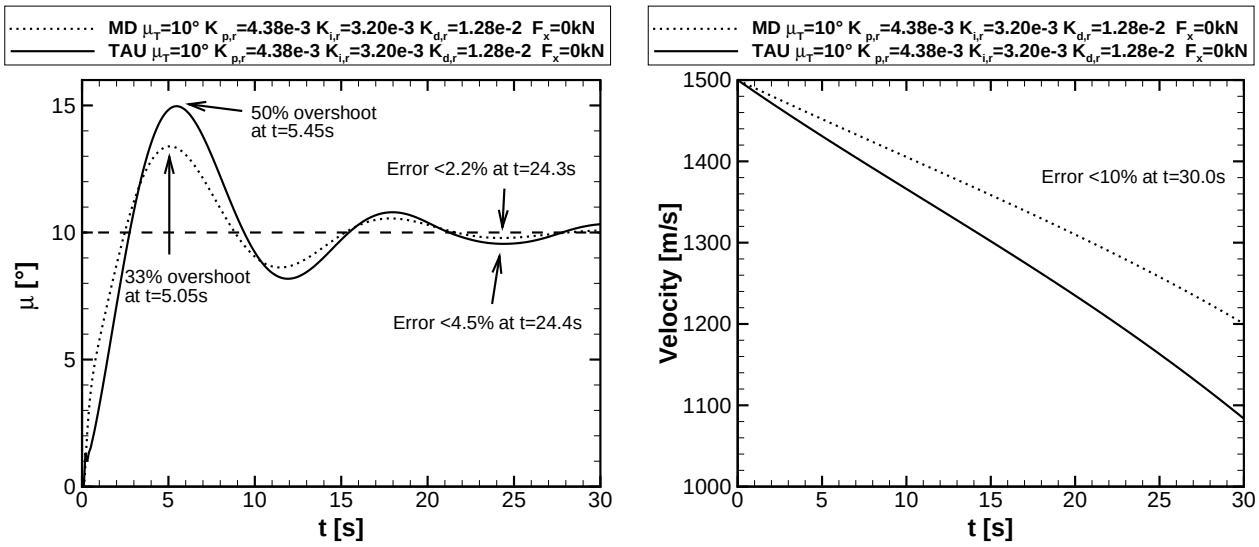

(a) Roll motion answer.

(b) Velocity development over time.

Figure 11: Roll motion answer compared by two coupling schemes RT and RMD.

3.2 Control of the Pitching Motion

Figure 12(a) describes a similar control response time for the pitching motion as shown in the preceding section. The solid line shows a stable answer after an initial deflection, same for the dashed and dotted lines. As the controlled motions can be superimposed besides the pitching motion the dotted lines have an overlain rolling motion as discussed in section 3.1.

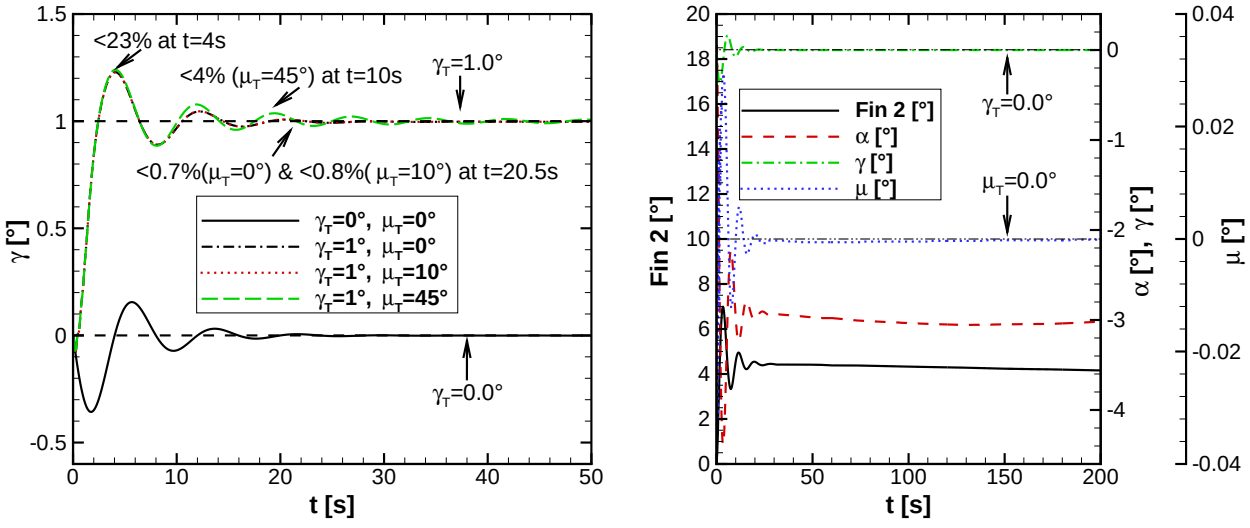

(a) Pitch motion answer.

(b) Example pitching motion of the vehicle.

Figure 12: Roll motion answer compared by two coupling schemes RT and RMD.

It can be seen that increasing rolling angles lead to increasing response times, because the aerodynamic efficiency

DOI: 10.13009/EUCASS2017-91

of the fins get reduced for the pitching maneuver. The worst case scenario is shown in a green dashed line with a rolling angle of $\mu_T = 45°$ at which the controller performs good.

Figure 12(b) illustrates a controlled pitching maneuver with a target flight path angle $\gamma_T = 0°$ and thrust of $F_x = 5kN$, i.e. the controller holds the vehicle at an constant flight path angle in an horizontal flight condition with a steady increasing velocity. In parallel the rolling angle μ is controlled to zero. The PID controller works perfectly, showing a small response time at the beginning of the run, holding γ afterwards close to zero even though the rocket is descending due to gravity effects. The resulting angle of attack of $\alpha = -3°$ is explained by the balance of gravitational force which drags the vehicle downwards and the vertical components of thrust as well as lift force of the vehicle which pulls it in upwards direction. The angle of attack is negative because of the coordinate system convention as the vehicle is flying at the southern hemisphere. The horizontal fin deflection angle varies in a small range smaller than $\eta_2 = 7.0°$.

3.3 Control of the Flight Path

After the shown rolling and pitching motion the controller gets expanded to a flight path controller, adding the horizontal flight path heading angle χ.

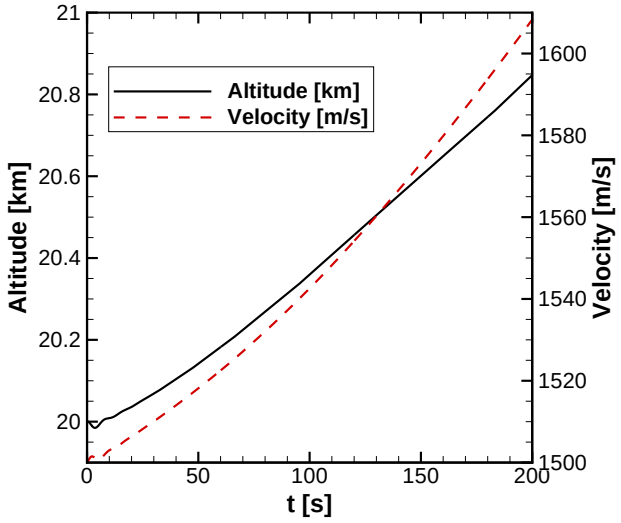

(a) Altitude and velocity over time.

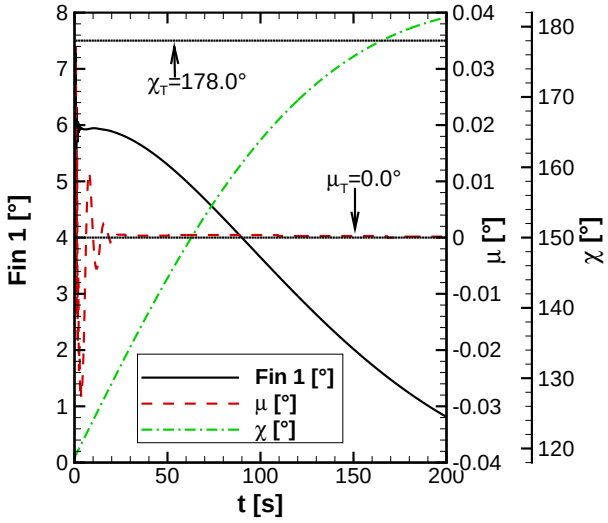

(b) Yawing and rolling motion.

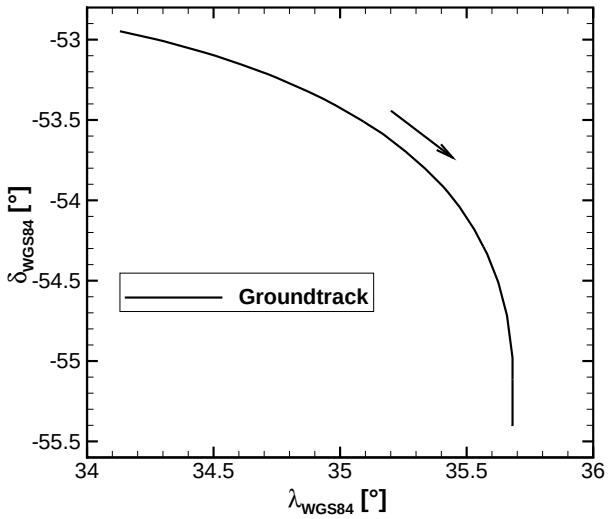

(c) Groundtrack.

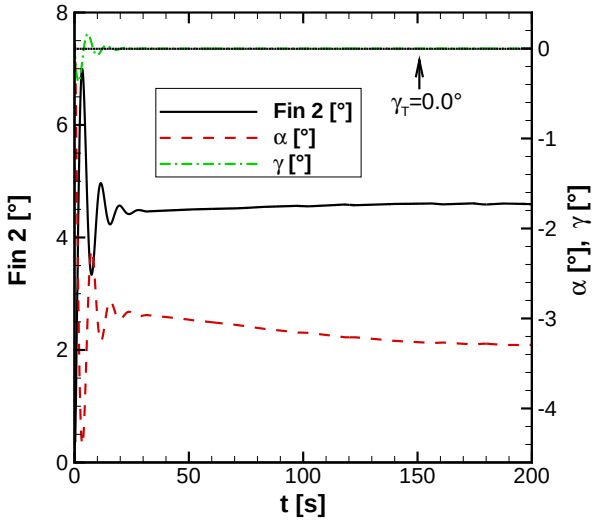

(d) Pitching motion.

Figure 13: Right curve.

Figure 13 illustrates a fully six DOF controlled flight of a right curve as the heading angle raises from 118° to

DOI: 10.13009/EUCASS2017-91

178°, shown in figure 13(b). Simultaneously the rolling angle μ_T as well as the flight path angle γ_T are kept at 0°, resulting in an upright horizontal flight curve shown in figure 13(c).

Due to the thrust of F_x=5kN the velocity is increasing. The raising altitude can be explained by the used reference ellipsoid WGS84 implemented in REENT. Moving with a flight path angle $\gamma_T = 0°$ from the equator to the poles of the earth means approaching to the semi-minor of the ellipse and therefore the flight altitude increases.

The described effect can be seen in figure 14 for the left curve as well. The altitude reduces until the point where the flight path heading angle χ passes 90° (figure 14(b)) and the ground track (figure 14(c)) points towards northern direction. Then the altitude reduces because the vehicle is flying in the direction of the equator. Similarly to the flown right curve the roll angle μ_T and flight path angle γ_T are set to zero whereas the flight path heading angle χ_T is controlled from 118° to 58°. The small drop in altitude shown in 13(a) and 14(a) at the beginning of the controlled curve describes the earlier mentioned initial unsteady starting point for the PID controller. Otherwise the resulting controller amplitudes at the beginning would be very small.

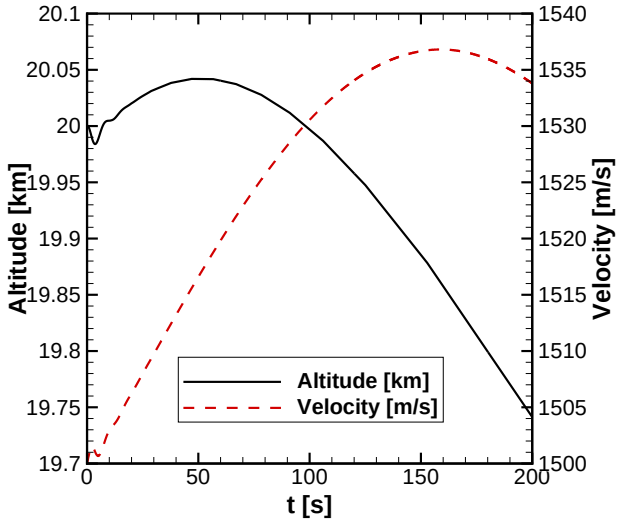

(a) Altitude and velocity over time.

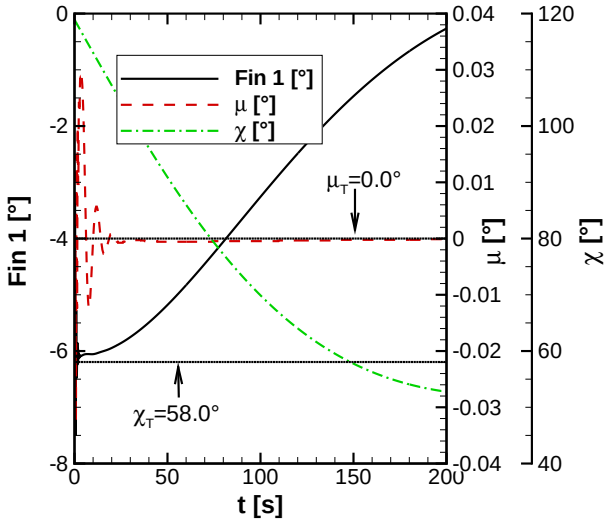

(b) Yawing and rolling motion.

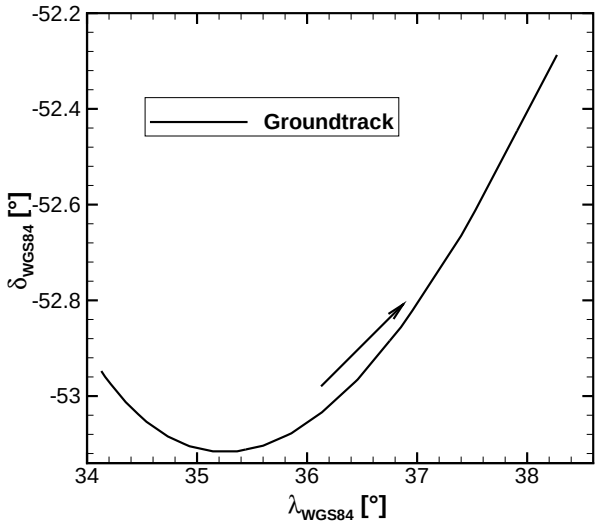

(c) Groundtrack.

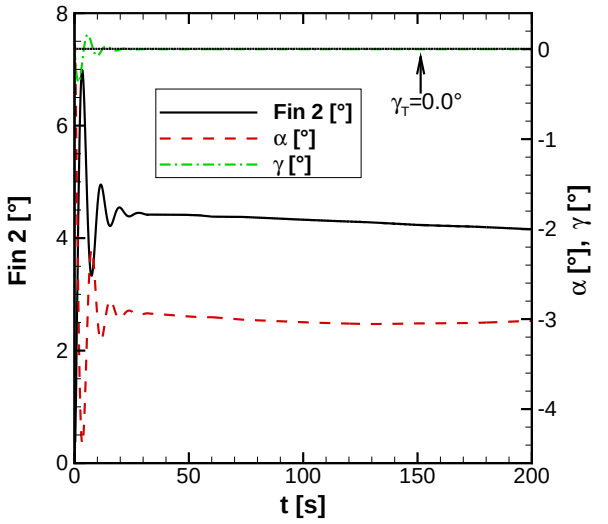

(d) Pitching motion.

Figure 14: Left curve.

DOI: 10.13009/EUCASS2017-91

4. Conclusions and Outlook

The present paper proves that the concept of interchangeable flow solvers is valid and that it can save much time to develop a controller in a low-fidelity solver and then apply it regularly in a more advanced high-fidelity solver.

This was presented by designing a PID controller using a coupled procedure of Reent-Missile DATOM for roll and pitch maneuvers and afterwards compare them with a Reent-DLR TAU coupling. The differences between the two models are small, which is mainly justified by the very simple flow conditions, where the low-fidelity method Missile DATCOM is still applicable. Afterwards the controller gets upgraded to a fully six DOF flight path controller flying some curved maneuvers. The coupled procedure then includes rather complex effects like the force connection between thrust, aerodynamic drag, velocity and gravitation at a certain altitude over the flown path.

In the near future it is planned to extend the complexity of the test cases to body-body interactions and fully controlled separation maneuvers. Here the high-fidelity approach is required as the solution automatically covers the full interactions of multi-body problems.

5. Acknowledgments

Sincere thanks go to Barbara Buffetti (DLR, German Aerospace Center) for her meshing contributions.

References

[1] William B. Blake. Missile Datcom, User Manual, AFRL-VA-WP-TR-1998-3009. Technical Report December 1997, Air Force Research Laboratory, Air Vehicles Directorate, Wright-Patterson Air Force Base, Ohio, 45433-7531, 1998.

[2] Johannes Burkhardt. *Konzeptioneller Systementwurf und Missionsanalyse für einen auftriebsgestützten Rückkehrkörper*. PhD thesis, University of Stuttgart, 2001.

[3] Javier Bartolome Calvo, Stephan Wolkow, and Thino Eggers. Application of a Coupling of Flight Mechanics and Aerodynamics to predict the SHEFEX I Ascent Phase. *New Results in Numerical and Experimental Fluid Mechanics*, 8(121):67–74, 2013.

[4] M Costello and J Sahu. Using computational fluid dynamic/rigid body dynamic results to generate aerodynamic models for projectile flight simulation. *Proceedings of the Institution of Mechanical Engineers, Part G: Journal of Aerospace Engineering*, 222:1067–1079, 2008.

[5] Thino Eggers and Michael Gräßlin. Layout of Hypersonic Vehicles by Coupling of Aerodynamics and Flightmechanics. *2nd International ARA Days*, (October), 2008.

[6] C. Farhat and M. Lesoinne. Two Efficient Staggered Algorithms for the Serial and Parallel Solution of Three-Dimensional Nonlinear Transient Aeroelastic Problems. *Computer Methods in Applied Mechanics and Engineering*, 182:499–515, 2000.

[7] Marius Franze. SHEFEX II - A First Aerodynamic and Atmospheric Post-Flight Analysis. *AIAA Atmospheric Flight Mechanics Conference*, (January):1–11, 2016.

[8] A E Hedin. Extension of the Msis Thermosphere Model in@Bullet the Middle and Lower Atmosphere. *Journal of Geophysical Research*, 96(A2):1159–1172, 1991.

[9] Ralf Heinrich and Andreas Michler. Unsteady Simulation of the Encounter of a Transport Aircraft with a Generic Gust by CFD Flight Mechanics Coupling. In *Proceedings of the CEAS conference*, Manchester, United Kingdom, 2009.

[10] A. Mack and Volker Hannemann. Validation of the Unstructured DLR-TAU-Code for Hypersonic Flows. *32nd AIAA Fluid Dynamics Conference and Exhibit, AIAA Paper 2002-3111*, pages 1–9, 2002.

[11] J Sahu and F Fresconi. Flight Behaviors of a Complex Projectile using a Coupled CFD-based Simulation Technique: Free Motion. *34th AIAA Applied Aerodynamics Conference*, (June):1–21, 2015.

[12] Jubaraj Sahu, Frank Fresconi, and Karen R. Heavey. Unsteady Aerodynamic Simulations of a Finned Projectile at a Supersonic Speed with Jet Interaction. *32nd AIAA Applied Aerodynamics Conference*, (June):1–35, 2014.

DOI: 10.13009/EUCASS2017-91

[13] Dieter Schwamborn, Thomas Gerhold, and Ralf Heinrich. The DLR TAU-Code: Recent Applications in Research and Industry. *European Conference on Computational Fluid Dynamics, ECCOMAS CFD*, pages 1–25, 2006.

[14] Sidra I. Silton, Jubaraj Sahu, and Frank Fresconi. Comparison of Uncoupled and Coupled CFD-based Simulation Techniques for the Prediction of the Aerodynamic Behavior of a Complex Projectile. *34th AIAA Applied Aerodynamics Conference*, (June):1–23, 2016.

[15] Thomas J Sooy and Rebecca Z Schmidt. Missile DATCOM (97) and Aeroprediction 98 (AP98). *Journal of Spacecraft and Rockets*, 42(2), 2005.

[16] Icao Standard, Atmosphere To, Proposed Extension To, and Tablesdata To. U.S. Standard Atmopshere 1962. Technical report, National Aeronautics and Space Administration, United States Air Force, United States Weather Bureau, 1962.

[17] Steven R Vukelich, Stan L Stoy, Keith A Burns, Joseph A Castillo, and Marvin E Moore. Missile Datcom, Volume I - Final Report, AFWAL-TR-86-3091. Technical report, McDonnell Douglas Missile Systems Company, Saint Louis, Missouri, 1988.

[18] Steven R Vukelich, Stan L Stoy, and Marvin E Moore. Missile Datcom, Volume II - User's Manual, AD-A210 128. Technical report, McDonnell Douglas Missile Systems Company, Saint Louis, Missouri, 1988.

[19] Yasuhiro Wada and Meng-Sing Liou. A flux splitting scheme with high-resolution and robustness for discontinuities. *AIAA paper 94-0083*, pages 1–23, 1994.

[20] J. G. Ziegler and N. B. Nichols. Optimum Settings for Automatic Controllers. *Journal of Dynamic Systems, Measurement, and Control*, 115(2B):220, 1993.